



HAL
open science

Preconditioned Krylov subspace methods for solving radiative transfer problems with scattering and reflection

Mohd Afeef Badri, Pierre Jolivet, Benoit Rousseau, Y. Favennec

► To cite this version:

Mohd Afeef Badri, Pierre Jolivet, Benoit Rousseau, Y. Favennec. Preconditioned Krylov subspace methods for solving radiative transfer problems with scattering and reflection. *Computers & Mathematics with Applications*, 2019, 77 (6), pp.1453-1465. 10.1016/j.camwa.2018.09.041 . hal-02333906

HAL Id: hal-02333906

<https://hal.science/hal-02333906>

Submitted on 14 Jan 2021

HAL is a multi-disciplinary open access archive for the deposit and dissemination of scientific research documents, whether they are published or not. The documents may come from teaching and research institutions in France or abroad, or from public or private research centers.

L'archive ouverte pluridisciplinaire **HAL**, est destinée au dépôt et à la diffusion de documents scientifiques de niveau recherche, publiés ou non, émanant des établissements d'enseignement et de recherche français ou étrangers, des laboratoires publics ou privés.

Preconditioned Krylov subspace methods for solving radiative transfer problems with scattering and reflection

M. A. Badri^{a,b}, P. Jolivet^c, B. Rousseau^b, Y. Favennec^{b,*}

^a*Institut de Recherche Technologique Jules Verne, 44340 Bouguenais, France*

^b*CNRS, Laboratoire de Thermique et Énergie de Nantes, 44306 Nantes, France*

^c*CNRS, Institut de Recherche en Informatique de Toulouse, 31062 Toulouse, France*

Abstract

Two Krylov subspace methods, the GMRES and the BiCGSTAB, are analyzed for solving the linear systems arising from the mixed finite element discretization of the discrete ordinates radiative transfer equation. To increase their convergence rate and stability, the Jacobi and block Jacobi methods are used as preconditioners for both Krylov subspace methods. Numerical experiments, designed to test the effectiveness of the (preconditioned) GMRES and the BiCGSTAB, are performed on various radiative transfer problems: (i) transparent, (ii) absorption dominant, (iii) scattering dominant, and (iv) with specular reflection. It is observed that the BiCGSTAB is superior to the GMRES, with lower iteration counts, solving times, and memory consumption. In particular, the BiCGSTAB preconditioned by the block Jacobi method performed best amongst the set of other solvers. To better understand the discrete systems for radiative problems (i) to (iv), an eigenvalue spectrum analysis has also been performed. It revealed that the linear system conditioning deteriorates for scattering media problems in comparison to absorbing or transparent media problems. This conditioning further deteriorates when reflection is involved.

Keywords: radiative transfer equation, specular reflection, mixed finite elements, preconditioning, Krylov solver, GMRES, BiCGSTAB

*Corresponding author.

Email address: `Yann.Favennec@univ-nantes.fr` (Y. Favennec)

1. Introduction

Radiative transfer problems are often solved by discretizing the radiative transfer equation (RTE), an equation that is integro-differential by nature [1]. As a consequence, one solves a large linear system $AI = b$, where A is a real matrix, and I and b are vectors. Depending on the chosen discretization, A can be symmetric, nonsymmetric, sparse or dense. For example, the spherical harmonics method (P_1 method) coupled to the finite volume method yields a symmetric system, cf. [2]. Other discretizations generating symmetric systems include the discrete ordinates method (DOM) coupled to the least square finite element method [3] or the simplified spherical harmonics method (SP_N method) coupled to the finite element method is used [4]. However, when the DOM is coupled to the finite volume method [5], or to the discontinuous Galerkin finite element method [6], then the obtained systems are nonsymmetric. In this article we employ the discrete ordinates method [7] coupled with the stabilized mixed finite element method [8] (DOM-FEM) for assembling the coefficient matrix A as well as the right-hand side vector b . These discretizations yield a sparse and nonsymmetric linear system.

The chosen DOM-FEM discretization, at present, is one of the widely used discretization techniques for radiative transfer problems. It provides accurate results for a vast range of radiation problems at moderate computational requirements. Complex geometries [9], heterogeneous media [10], reflections [11], anisotropic scattering [12], etc., can be easily handled by the DOM-FEM method, making it a versatile RTE discretization technique. To summarize how the DOM-FEM discretization for the RTE works, the DOM firstly transforms the integro-differential RTE into a set of coupled partial differential equations (PDEs). Then, the stabilized mixed FEM is applied over all partial differential equations. Finally, we derive $AI = b$. More details may be found in [13, 14]. For radiative transfer, solution strategies of such linear systems have been developed using the operator-split strategy which reduces the coupled system problem to the solution of a series of linear problems. This method is more commonly known as the source-iteration method [15]. However, when one considers radiative transfer problems with dominant scattering, reflection, and heterogeneities, such a solution technique leads to unacceptably slow convergence rates, or may even fail to converge [16]. As a remedy to the slow convergence rates for the scattering dominant problems, the diffusion synthetic acceleration method may be used, cf. [17]. Such a

method can be seen as a preconditioned source-iteration method, and helps in accelerating the convergence rate for most highly scattering problems.

In the recent years, many researches have used Krylov subspace methods [18] as an alternative to the traditional source-iteration method or to the diffusion synthetic acceleration method. These Krylov subspace methods guarantee fast convergence for the non-trivial radiative transfer problems (some of which were mentioned in the preceding paragraph), without any need for deriving sophisticated acceleration techniques [19, 20, 21, 5, 22]. Furthermore, recent advancements in parallelism of the Krylov subspace methods have provided the computational community with open-source mathematical libraries that scale well, and can handle large linear systems, cf. [23, 24]. Such tools provide easy access to a collection of Krylov subspace solvers and preconditioners that can be suitably selected depending on the system to be solved. In this article, we use such an open-source mathematical library, PETSc [23], to solve the linear systems that arise in the DOM-FEM discretization of the RTE.

In this study, we used two Krylov subspace methods, the BiCGSTAB [25] and the GMRES [26], with and without preconditioning, for radiative transfer problems with specular reflection at the boundaries. To argue in favor of Krylov subspace solvers for solving such radiative problems, an eigenvalue spectrum analysis (based on the Arnoldi iteration algorithm [27]) has been performed for different transparent, absorbing, scattering, and reflecting radiation problems. By computing the condition number based on this eigenvalue analysis, we show its degradation when reflection phenomena are involved.

To sum up the remainder of this article, the upcoming section 2 introduces the discrete ordinates RTE with different boundary conditions. Next, section 3 discusses the linear system that arises from the DOM-FEM discretization of the RTE. Section 3 also provides a quick overview of solution methodologies for solving such systems. Section 4 then presents the numerical results along with discussions based on eigenspectra for various radiation problems. Section 4 further presents a comparative performance analysis of the GMRES and the BiCGSTAB, for solving some complex radiative transfer problems. We draw a quick conclusion in section 5.

2. Problem formulation

In this article, we consider the discrete form of the monochromatic steady-state RTE [7], stated on a bounded domain $\mathcal{D} \subset \mathbb{R}^3$. After applying the DOM, the radiative transfer model contains a set of N_d coupled partial differential equations, for which the m th equation reads,

$$\mathcal{R}_m = (\mathbf{s}_m \cdot \nabla + \beta) I_m(\mathbf{x}) - \sigma_s \sum_{n=1}^{N_d} \omega_n I_n(\mathbf{x}) \Phi(\mathbf{s}_m, \mathbf{s}_n) - \kappa I_b(\mathbf{x}) = 0. \quad (1)$$

The equation (1), written for all $m = 1, \dots, N_d$, forms a set that statistically describes the interaction of radiation using discrete radiative intensities I_m , each I_m propagating towards its own direction \mathbf{s}_m . For each \mathcal{R}_m , there occurs: radiation loss due to extinction $\beta I_m(\mathbf{x})$, radiation gain due to in-scattering $\sigma_s \sum_{n=1}^{N_d} \omega_n I_n(\mathbf{x})$, and radiation gain due to black-body emission $\kappa I_b(\mathbf{x})$. The remaining symbols present within (1) are, the extinction coefficient $\beta = \kappa + \sigma_s$, the absorption coefficient κ , the scattering coefficient σ_s , the scattering phase function $\Phi(\mathbf{s}_m, \mathbf{s}_n)$, and the Planck black-body function I_b , which in turn depends on the spatial temperature distribution T within the medium. Lastly, N_d and ω are the total number of angular directions and the weights associated to these directions, respectively.

To complete the problem definition, boundary conditions containing external sources and reflections at the domain boundary $\partial\mathcal{D} \cap (\mathbf{s}_m \cdot \mathbf{n} < 0)$ (with \mathbf{n} being the outward unit normal vector), are given by,

$$I_m(\mathbf{x}) = \hat{I}_m(\mathbf{x}) + (1 - \alpha) I_m^\ominus(\mathbf{x}) + \alpha I_m^\vee(\mathbf{x}) \quad \forall \mathbf{x} \in \partial\mathcal{D}. \quad (2)$$

Here, $\hat{I}_m(\mathbf{x})$ is the Dirichlet contribution due to external sources or diffused loading, $I_m^\ominus(\mathbf{x})$ quantifies the diffused contribution of reflection, $I_m^\vee(\mathbf{x})$ is the specular contribution of the reflection, and $\alpha \in [0, 1]$ is a coefficient weighting the two reflection contributions. The diffused and the specular reflections are further expanded as,

$$I_m^\ominus(\mathbf{x}) = \frac{\rho_d}{\pi} \sum_{\mathbf{s}_j \cdot \mathbf{n} > 0} \omega_j I_j(\mathbf{x}) \mathbf{s}_j \cdot \mathbf{n} \quad \text{and} \quad I_m^\vee(\mathbf{x}) = \rho_s(\mathbf{s}_m, \mathbf{n}) \sum_{\mathbf{s}_j \cdot \mathbf{n} > 0} \delta_{m,j}(\mathbf{n}) I_j(\mathbf{x}).$$

The symbols ρ_s and ρ_d are the specular and the diffuse reflectivity coefficients, respectively, and $\delta_{m,j}$, for all $(m, j) \in \llbracket 1; N_d \rrbracket^2$, are the partition-ratio

coefficients. The way these coefficients are calculated in a very accurate manner for specular reflection is presented for two- and three-dimensional problems in [6] and [11], respectively. In particular, $\delta_{m,j}$ is calculated using the so-called “partitioning method” [11]. Note that the weighting coefficient α is assumed to be equal to 1 in this study, i.e., only specular reflection is considered.

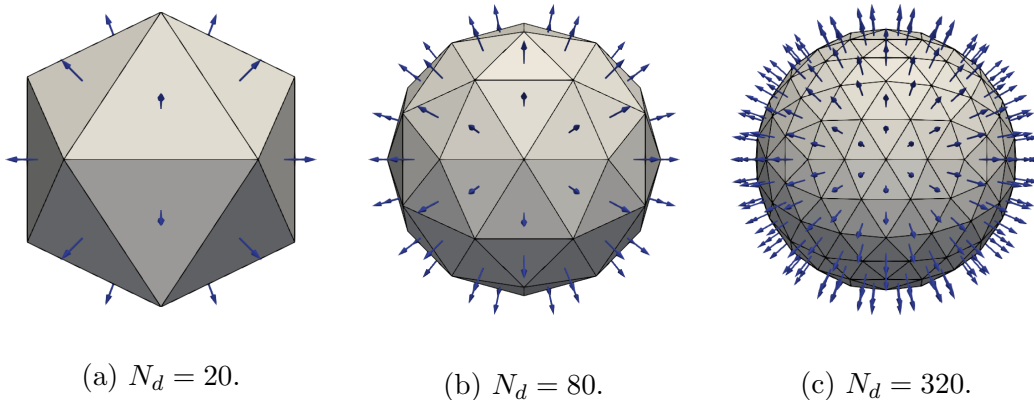


Figure 1: Discretized angular space with the icosahedron refinements. (a) icosahedron, (b) first refinement icosahedron, and (c) second refinement icosahedron.

Recently, we introduced the mixed finite element method (with the SUPG stabilization) for solving the discrete ordinates RTE (1) [13, 14]. The solver was parallelized using either domain decomposition or angular decomposition. In these previous studies, the reflection phenomena were not integrated in the solver. However for the current study here, the equation set (1) is solved using this (parallel) mixed finite element based solver, with the added capabilities of modeling specular reflection using the partitioning method. To detail the solver further, it is interfaced with the open-source mathematical library PETSc, which offers a suite of Krylov subspace methods along with preconditioners, for solving the consequent linear systems in parallel, using distributed-memory parallelism through the Message Passing Interface (MPI). The discretization kernel uses unstructured (tetrahedral) meshes for space \boldsymbol{x} , and the refined icosahedron sphere discretization for directions \boldsymbol{s} . Figure 1 shows the icosahedron, the first refinement icosahedron, and the second refinement icosahedron, these correspond to $N_d = 20, 80$, and 320 , respectively.

3. The finite element linear system

3.1. Assembling the linear system

As mentioned earlier, the linear system arising from the finite element discretization of the discrete ordinates RTE is sparse and nonsymmetric by nature. It has the form:

$$AI = b, \quad (3)$$

with the matrix $A \in \mathbb{R}^{m \times m}$ and the vectors $I \in \mathbb{R}^m$ and $b \in \mathbb{R}^m$. The symbol $m = N_d \times N_v$, N_v being the number of degrees of freedom associated with the spatial discretization. To analyze thoroughly the linear system, we derive the following block matrix splitting using the angular approach presented in [14], for the linear system (3).

$$AI \triangleq [A^T + A^E + A^S + A^R] I = b, \quad (4)$$

with, A^T , A^E , A^S , and A^R representing, respectively, the contributions from transport, extinction, scattering, and reflection processes embedded within the RTE (1). These are further expanded as,

$$A^T = \begin{pmatrix} A_1^T & 0 & 0 \\ 0 & \ddots & 0 \\ 0 & 0 & A_{N_d}^T \end{pmatrix}, \quad A^E = \begin{pmatrix} A_1^E & 0 & 0 \\ 0 & \ddots & 0 \\ 0 & 0 & A_{N_d}^E \end{pmatrix}, \quad (5)$$

$$A^S = \begin{pmatrix} A_{1,1}^S & \cdots & A_{1,N_d}^S \\ \vdots & \ddots & \vdots \\ A_{N_d,1}^S & \cdots & A_{N_d,N_d}^S \end{pmatrix}, \quad \text{and} \quad A^R = \begin{pmatrix} 0 & A_{1,2}^R & \cdots & A_{2,N_d}^R \\ A_{2,1}^R & 0 & \cdots & A_{1,N_d}^R \\ \vdots & \vdots & \ddots & \vdots \\ A_{N_d,1}^R & A_{N_d,2}^R & \cdots & 0 \end{pmatrix}. \quad (6)$$

Similarly, the vector b expands to $b = [b_1 \ \cdots \ b_{N_d}]$. The m th block of rows of the linear system is related to the finite element discretization of a single \mathcal{R}_m . It also includes, due to the integration by parts, the boundary condition terms. The entries of these matrices and the vector b are defined by,

$$[A_m^T]_{k,l} = - \int_{\Omega} \mathbf{s}_m \cdot \nabla \varphi_k (\varphi_l - \gamma \mathbf{s}_m \cdot \nabla \varphi_l) \, d\mathbf{x} + \int_{\substack{\partial\Omega \\ \mathbf{s}_m \cdot \mathbf{n} > 0}} \mathbf{s}_m \cdot \mathbf{n} \, \varphi_k \varphi_l \, d\mathbf{x}, \quad (7)$$

$$[A_m^E]_{k,l} = \int_{\Omega} \beta \varphi_l (\varphi_k + \gamma \mathbf{s}_m \cdot \nabla \varphi_k) \, d\mathbf{x}, \quad (8)$$

$$[A_{m,n}^S]_{k,l} = - \int_{\Omega} \sigma_s \omega_n \Phi(\mathbf{s}_m, \mathbf{s}_n) \varphi_l (\varphi_k + \gamma \mathbf{s}_m \cdot \nabla \varphi_k) \, d\mathbf{x}, \quad (9)$$

$$[A_{m,n}^R]_{k,l} = \int_{\substack{\partial\Omega \\ \mathbf{s}_n \cdot \mathbf{n} < 0 \cap \mathbf{s}_m \cdot \mathbf{n} > 0}} \rho_s(\mathbf{s}_m, \mathbf{n}) \delta_{m,n}(\mathbf{n}) \varphi_l \varphi_k \mathbf{s}_m \cdot \mathbf{n} \, d\mathbf{x}, \quad (10)$$

$$[b_m]_k = - \int_{\substack{\partial\Omega \\ \mathbf{s}_m \cdot \mathbf{n} < 0}} \hat{I}_m \varphi_k \mathbf{s}_m \cdot \mathbf{n} \, d\mathbf{x} + \int_{\Omega} \kappa I_b (\varphi_k + \gamma \mathbf{s}_m \cdot \nabla \varphi_k) \, d\mathbf{x}. \quad (11)$$

In this paper, the finite element basis functions φ_k , $k = 1, \dots, N_v$ are the first-order Lagrange polynomials, and the SUPG coefficient γ is chosen following [28]. Equations (7) to (11) combined together, correspond to the discrete formulation of equation (1) solved with the boundary conditions (2). More detailed derivations of the variational formulation may be found in [11, 14].

3.2. Solution methods for the linear system

The most common iterative solving techniques for the discrete ordinates RTE linear system (3), belong to the fixed-point iteration schemes given by,

$$I_{k+1} = I_k + C^{-1}(b - AI_k), \quad (12)$$

where the subscript k stands for the iteration index, and C^{-1} is the preconditioner. The source-iteration method, which is the most widely used method for solving the linear systems that arise from the discrete ordinates RTE, uses $C^{-1} = (A^T + A^E)^{-1}$. In fact, the source-iteration scheme can be seen as a Richardson method with “nearly” block Jacobi preconditioning (because the diagonal blocks from A^S are not used in C^{-1}). For absorption-dominant, or purely absorbing radiative transfer problems, this preconditioner forms a good approximation of A^{-1} , thereby the linear system (3) solved iteratively with the source-iteration method undoubtedly performs well. In other situations, for example if the radiative transfer problem is scattering-dominant,

or if it involves reflection, the source-iteration, or other fixed-point methods do not perform well.

Since the source-iteration method is a fixed-point iteration scheme, its convergence rate heavily relies on the spectral radius of the matrix $C^{-1}A$. In 1971, Reed [29] carried out the Fourier analysis for the source-iteration method, and proved that the spectral radius c_s of $C^{-1}A$ is independent of the spatial mesh and is equal to the ratio $\frac{\sigma_s}{\kappa}$. Hence, when $\sigma_s \gg \kappa$, the source-iteration method exhibits slow convergence. In Reed's paper it was also proved that, for the improved source-iteration scheme, namely the diffusion synthetic acceleration method, the spectral radius of $C^{-1}A$ was dependent on the spatial mesh size, which was characterized by the size h of the mesh elements. It was seen that meshes with h greater than the mean free path lead to divergence of such solvers.

Krylov subspace solvers, as alternatives to fixed-point methods, usually have better convergence rates. In practice, a Krylov subspace solver, from a guess I_0 and an initial residual $r_0 = b - AI_0$, computes a more accurate approximation of the solution vector I_k by using the Krylov subspace \mathcal{K}_k given by:

$$\mathcal{K}_k(A, r_0) = \text{span}\{r_0, Ar_0, A^2r_0, \dots, A^{k-1}r_0\}.$$

In other words, Krylov subspace methods solve $AI = b$ by repeatedly performing matrix–vector multiplications.

The GMRES and the BiCGSTAB are two different Krylov methods that may be used for solving the linear system $AI = b$ arising from the DOM-FEM discretization of the discrete ordinates RTE. These two methods can be differentiated based on how they use the Krylov space $\mathcal{K}_k(A, r_0)$ to generate the solution vector I_k . On the one hand, the GMRES chooses I_k by minimizing the Euclidean norm of the residual $r_k = b - Ax_k$ for x_k in $\mathcal{K}_k(A, r_0)$. It does so in two steps: at first, an orthogonal basis is generated by the Arnoldi procedure, and as a second step, a least squares problem is solved to compute I_k . The BiCGSTAB, on the other hand, tries to reach convergence by following the mutual orthogonalization of two sequences using the nonsymmetric Lanczos procedure. More details may be found in [30].

Concerning the stopping criterion, usually, convergence is assumed to be reached when the norm $\|r_k\|_2 = \|b - Ax_k\|_2$ is sufficiently small. Generally, the total number of iterations needed to reach convergence, k_c , is much lower than m , the order of A . How few iterations are required depends on the eigenspectrum of A , and the nature of this dependence is crucial for understanding Krylov subspace methods [18].

4. Results and discussions

In this section, results and discussions for different numerical tests are provided. The convergence for the Krylov subspace solvers is reached when the norm of the relative unpreconditioned residual $\|r_k\|_2 / \|r_0\|_2$ is lower than 10^{-6} .

The numerical experiments presented in the subsection 4.1 were performed on an ordinary laptop (Intel Core i7 with 16 GB of RAM) using 8 MPI processes in parallel, while the numerical experiments presented in the next subsection 4.2 were performed using 320 MPI processes on the supercomputer LIGER, at ICI supercomputing facility (6,048 cores Intel Xeon cluster) hosted by Central Nantes, France. In [14], we reported near-linear scaling for our parallel solvers. Hence, solver performances derived using a specific number of MPI processes (320 in this case), should have similar trends at other MPI counts as well because of the optimal scaling. Before advancing further, it is to be notified that the solvers used for the upcoming tests have been verified thoroughly using standard benchmarking procedures, see [14, 11]. Note also that, among the previously developed angular decomposition and domain decomposition parallel solvers [14], the former is used as the standard solver throughout this study.

4.1. Eigenspectrum analysis

The numerical experiments performed in this subsection are designed to study the eigenspectrum of different radiation problems. The Arnoldi iteration algorithm [27] is applied for calculating the eigenspectrum of the matrices. Note that, though a total of m eigenvalues exist for a matrix of size

m , the Arnoldi iteration algorithm only provides us with the N_{eigen} dominant eigenvalues, out of all eigenvalues. This incomplete spectrum cannot be used for complete eigenvalue analysis, however it is intended here only for assisting in understanding the convergence of the Krylov subspace solvers, and for approximating the matrix condition numbers.

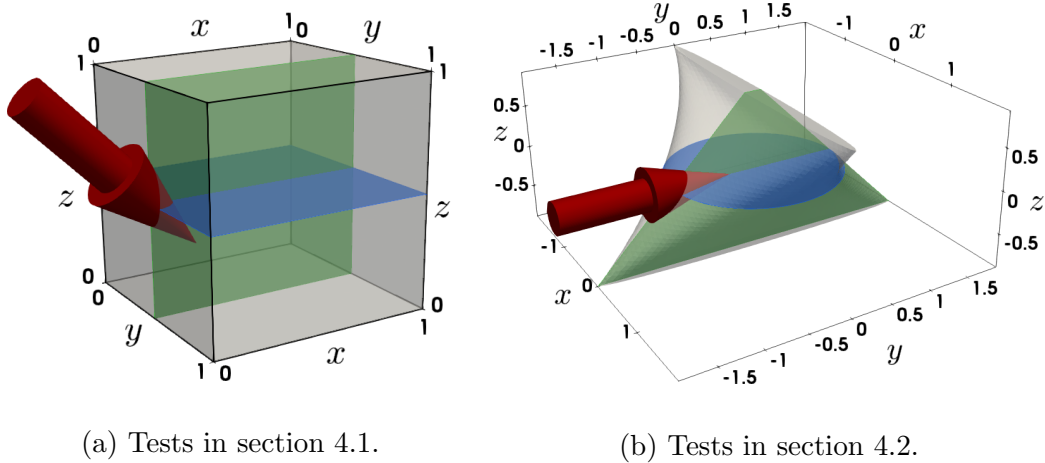


Figure 2: Dirichlet boundary conditions and the geometry used for the tests in section 4. External radiation source is shown impinging the different media.

For the numerical tests in this subsection, we used a 1 cm^3 cubic-shaped participating medium impinged with a top hat-type collimated external radiative source on its left face:

$$\hat{I}(\mathbf{x}, \mathbf{s}) = I_0 \mathbb{1}_{[(y-y_0)^2 + (z-z_0)^2 < r_b^2, x=0, \text{ and } \mathbf{s}=\mathbf{s}_{in}]}, \quad (13)$$

where $I_0 = 100 \text{ W cm}^{-2}$, $y_0 = 0.5 \text{ cm}$, $z_0 = 0.5 \text{ cm}$, and $r_b = 0.2 \text{ cm}$ represent the strength of the source, the center coordinates, and the impinging radius, respectively. $\mathbb{1}$ is the Heaviside step function such that $\mathbb{1}_{[\text{condition}]} = 1$ if the condition is true, and $\mathbb{1}_{[\text{condition}]} = 0$ otherwise. The impinging direction of this source is $\mathbf{s}_{in} = \left[\frac{-1}{\sqrt{2}} \frac{-1}{\sqrt{2}} 0 \right]^T$. A schematic representation of this Dirichlet boundary condition is shown in figure 2a. Further, a 10,000 nodes tetrahedral mesh and a 80 directions refined icosahedron (figure 1b) were used for the spatial and the angular meshes, respectively. The media are considered homogenized with $\Phi(\mathbf{s}_m, \mathbf{s}_n)$ modeled using the Henyey–Greenstein phase function [31], with the anisotropy factor $g = 0.5$. Based on this geom-

etry and boundary condition, eight tests (1A to 1H) are formulated with the different radiation parameters summarized in table 1.

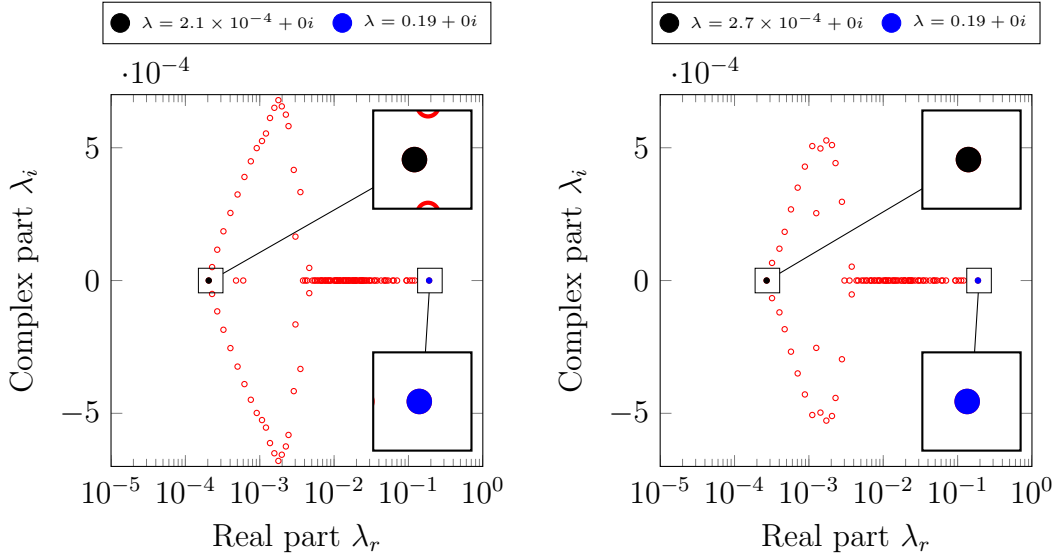
Test	κ	σ_s	n	Comments
1A	ϵ	ϵ	1	Transparent medium without reflection
1B	5	ϵ	1	Highly absorbing medium without reflection
1C	1	1	1	Semi-transparent medium without reflection
1D	ϵ	5	1	Highly scattering medium without reflection
1E	ϵ	ϵ	2.5	Transparent medium with reflection
1F	5	ϵ	2.5	Highly absorbing medium with reflection
1G	1	1	2.5	Semi-transparent medium with reflection
1H	ϵ	5	2.5	Highly scattering medium with reflection

Table 1: Radiative properties for tests 1A to 1H used in section 4.1: absorption coefficient κ (in cm^{-1}), scattering coefficient σ_s (in cm^{-1}), and index of refraction n of the medium. The small value ϵ is set to 10^{-6} .

Figure 3a presents the eigenspectrum for test 1A, which considers a non-reflecting transparent medium. The linear system conditioning in this case is dominated by the transport matrix A^T , as $A^S \approx 0$, $A^E \approx 0$, and $A^R = 0$. As such, the linear system is diagonally dominant. Based on the highest and the lowest eigenvalues (marked with filled black and blue circles in the plot of figure 3a, respectively), we get an approximate condition number $\text{cond}_2(A) = \max |\lambda(A)| / \min |\lambda(A)| \approx 921$.

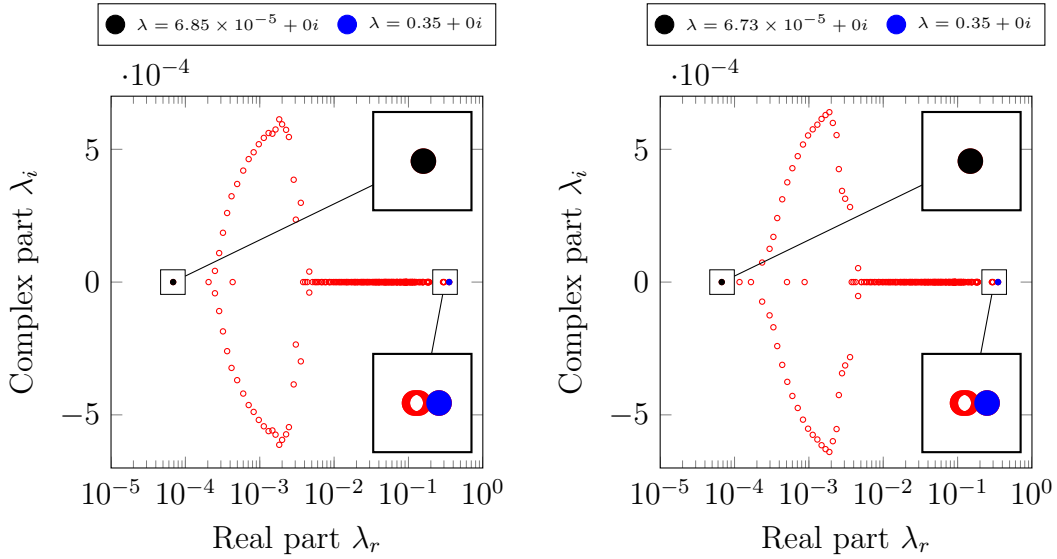
Figure 3b presents the eigenspectrum for test 1B, which considers a non-reflecting optically thick medium (strong absorption). The linear system conditioning in this case is dominated by both the transport A^T and the extinction A^E , as $A^S \approx 0$ and $A^R = 0$. As weights are added to the diagonal matrices, we expect a better conditioning than for the transparent test 1A. This is proved by a reduction of the condition number $\text{cond}_2(A) \approx 695$. Comparing to test 1A, there is a 30% smaller value. The Krylov subspace methods may be expected to converge in fewer iterations.

Next, for tests 1C and 1D, cases that involve scattering, the eigenspectra are presented in figures 3c and 3d, respectively. Notice the drift of minimal eigenvalues towards the origin, in comparison to the transparent and absorption test cases. $\min |\lambda|$ are observed to be approximately four times smaller compared to the previous tests. The highest eigenvalues $\max |\lambda|$ are also



(a) Transparent medium, test 1A.

(b) Highly absorbing medium, test 1B.



(c) Semi-transparent medium, test 1C.

(d) Highly scattering medium, test 1D.

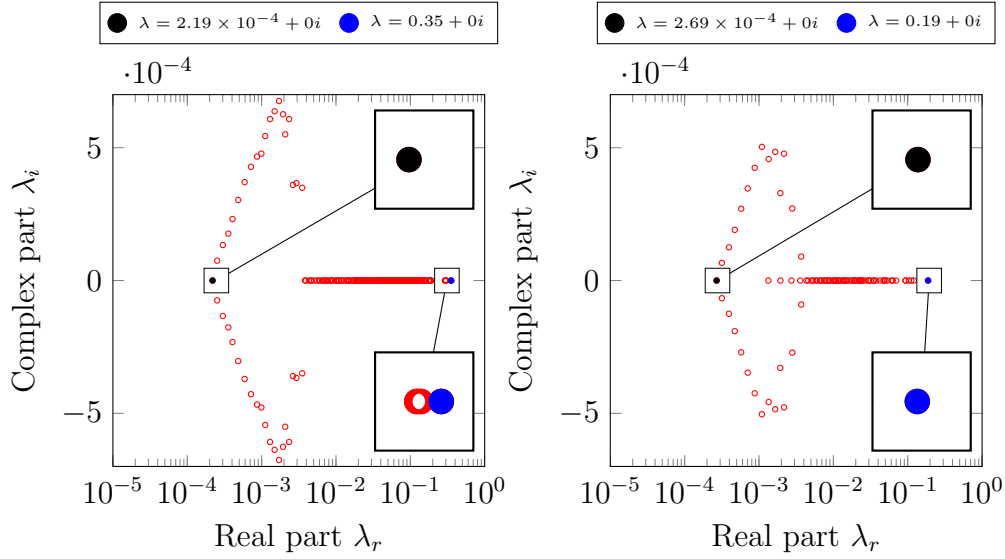
Figure 3: Eigenspectra for the transparent (pure transport) medium (test 1A), for the highly absorbing (optically thick) medium (test 1B), for the semi-transparent medium (test 1C), and for the highly scattering medium (test 1D). For this whole set of tests, the refractive index n was set to 1 (non-reflecting media).

observed to increase in magnitude, however by a factor two only. Overall, these drifts of eigenvalues result in increasing the condition numbers. We determined $\text{cond}_2(A) \approx 5,155$ for test 1C and $\text{cond}_2(A) \approx 5,197$ for test 1D. Hence, it is likely that a larger Krylov subspace (in dimension) would be needed for solving the scattering media problems.

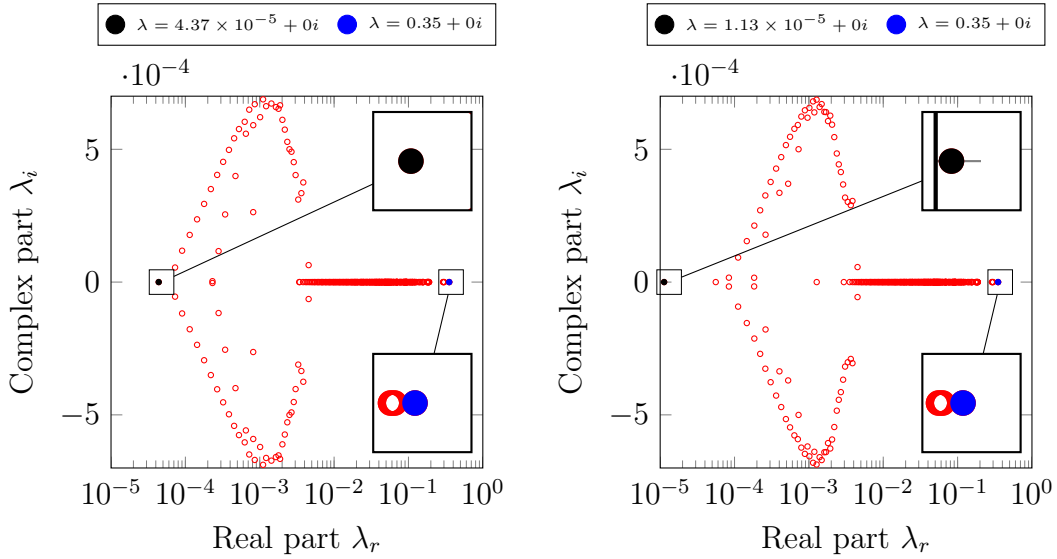
Another perspective to understand the increase in $\text{cond}_2(A)$ for tests 1C and 1D is that, due to the presence of the scattering phenomenon ($\sigma_s \geq 0$), the N_d discrete PDEs in (1) become strongly coupled, hence the global system is more difficult to solve. More specifically, now the solver has to deal with $A = A^T + A^E + A^S$. Unlike matrices A^T and A^E , which just contain diagonal blocks, the scattering matrix A^S contains both diagonal and off-diagonal blocks, cf. equations (5) and (6). Indeed, it is the presence of A^S which causes the strong coupling and the increase of the condition number.

Tests 1E, 1F, 1G, and 1H are similar to tests 1A, 1B, 1C, and 1D, respectively, except that for these tests, specular reflection is allowed at the boundaries. The corresponding spectra for the tests 1E to 1H are presented in figures 4a to 4d, respectively. Observe that the eigenspectrum for test 1F (figure 4b) is almost similar to its corresponding non-reflecting test 1B (figure 3b). More precisely, we report that $\text{cond}_2(A) \approx 699$ for test 1F, which is almost similar to what was reported for test 1B, where $\text{cond}_2(A) \approx 695$. Due to such a similarity between the systems, ideally both tests 1B and 1F should converge almost with similar rates. The reason for this similarity is that, due to the strong absorption coefficient for test 1F, the impinging radiation is not able to reach any other boundary of the medium. The impinging radiation, in fact, would be absorbed as soon as it enters the medium, hence not allowing for reflection physics to occur. Thereby, we could say that, even though the physics of reflection is present in test 1F, its eigenspectrum is still mostly controlled by the transport A^T and the extinction A^E .

From the eigenspectrum of test 1E, which considers a transparent medium with reflection at boundaries, it is seen that adding reflection alone to the transport can lead to a change of the matrix condition number. In particular, the greatest eigenvalue was observed to increase (by a factor of two in comparison to the pure transport case), while the smaller eigenvalue remained stable. Overall, $\text{cond}_2(A) \approx 1,598$, which is 1.7 times greater than that of the non-reflecting transparent medium case (test 1A).



(a) Transparent medium, test 1E. (b) Highly absorbing medium, test 1F.



(c) Semi-transparent medium, test 1G. (d) Highly scattering medium, test 1H.

Figure 4: Eigenspectra for the transparent (pure transport) medium (test 1E), for the highly absorbing (optically thick) medium (test 1F), for the semi-transparent medium (test 1G), and for the highly scattering medium (test 1H). For this whole set of tests, the refractive index n was set to 2.5 (highly reflective borders).

Coming to the scattering tests with reflection, tests 1G and 1H, we observe a drift of low eigenvalues towards the origin when compared to their counterpart tests 1C and 1D. In particular, the smallest eigenvalue was 1.6 and 6 times smaller for tests 1G and 1H, respectively, than what was observed for scattering tests without reflection. However the highest eigenvalue remains stable, indicating that it is not influenced by the presence of reflection. Overall, the $\text{cond}_2(A) \approx 8,046$ and $30,973$ for tests 1G and 1H, respectively. Comparing to other problems in this subsection, the condition number observed for the highly scattering problem involving reflection (test 1H) is the highest in magnitude. Hence, it is likely that a larger Krylov subspace (in dimension) would be needed for solving this problem.

To explain in more details the reflecting tests, physically dealing with specular reflection can be tricky because, at the reflecting border, the energy carried by the impinging direction i is assigned to the reflecting direction(s) j . The reflecting direction(s) j depends both on the surface normal \mathbf{n} and on the direction of incidence. For geometries with complex boundaries (many distinct normals) the probability of i getting reflected to many arbitrary directions j is high. Owing to this physics, the reflecting matrix A^R contains an arbitrary weighted structure which is contrary to the uniform weighted structure of other matrices present in expression (4). In other words, the coupling between the N_d PDEs (1) becomes less structured, hence more difficult to handle.

4.2. Krylov solver analysis for different radiation problems

Based on the eigenspectrum analysis carried out in the previous subsection, it was revealed that the absorbing media problems are well-conditioned, the condition number increases when scattering is involved, and becomes even worse when the medium is both scattering and reflecting. For this reason, in this subsection, we analyze five different problems, tests 2A to 2E, solved with the GMRES and the BiCGSTAB, with and without preconditioning. In particular, two classic preconditioners, the standard Jacobi and the block Jacobi (with incomplete LU factorizations with zero level of fill-in as block solvers) applied on the right, are used to enhance the efficiency of the two Krylov subspace methods.

For the tests of this subsection, a berlingot-shaped medium (see figure 2b) is used as the standard geometry. The non-convex geometry resembles a tetrahedron which is used to assimilate the cross-section between two struts of an open-cell foam, as used in concentrated solar power applications [11]. The surface topology $\partial\mathcal{D}(u, v)$ of the berlingot is parameterized by the following [32],

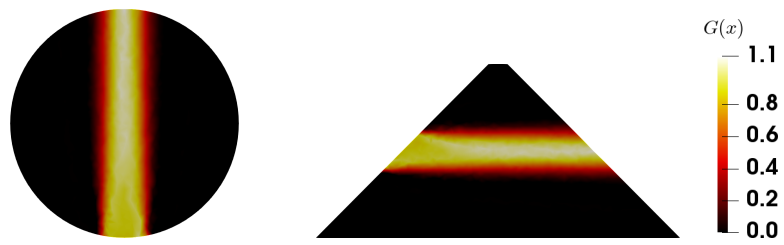
$$\partial\mathcal{D}(u, v) = \begin{cases} x = ab(1 + u) \cos v \\ y = ab(1 - u) \sin v \\ z = au \end{cases} \quad a, b \in \mathbb{R}, \quad u \in [-1, 1], \quad \text{and } v \in [0, 2\pi[,$$

in which a and b define the height and the width of the geometry, respectively. We have chosen $a = b = 1$, this corresponds to a berlingot-shaped medium which is 4 cm \times 4 cm \times 2 cm in dimensions.

Much like the boundary conditions used in the previous subsection, in this subsection the collimated top hat-type radiative source follows the same equation (13), but with the following parameters: $I_0 = 1 \text{ W cm}^{-2}$, $y_0 = 0.0 \text{ cm}$, $z_0 = 0.0 \text{ cm}$, $r_b = 0.2 \text{ cm}$, and $\mathbf{s}_{\text{in}} = [0 \ 1 \ 0]^T$, i.e., the source enters the geometry with its direction parallel to the y -axis. Figure 2b presents an isometric view of the berlingot-shaped medium and its corresponding Dirichlet boundary condition. The figure also contains internal cross-sections of the geometry in order to detail the berlingot's complex shape.

Further, a 57,000 nodes tetrahedral mesh and the 320 directions refined icosahedron (figure 1c) were used as the spatial and angular meshes, respectively. In this subsection, we would be dealing with problems involving reflection, to capture the physics more accurately such high count of directions ($N_d = 320$) was used, as recommended in [9]. Just like the tests in the previous subsection, the media are considered homogenized with $\Phi(\mathbf{s}_m, \mathbf{s}_n)$ modeled using the Henyey–Greenstein phase function, with the anisotropy factor $g = 0.5$. The five tests in this subsection, tests 2A to 2E, are formulated with the different radiation parameters summarized in table 2.

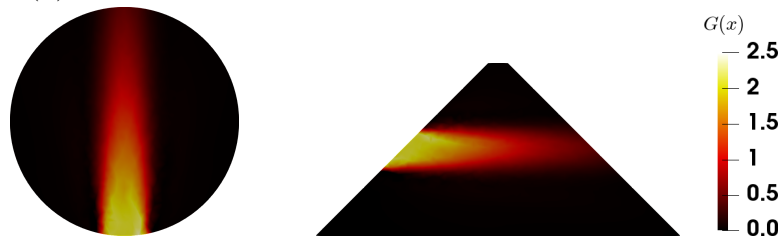
Figure 5 shows two cross-sections (xy -plane at $z = 0$ and yz -plane at $x = 0$) of the photon density fields, $G(\mathbf{x}) = \sum_{m=1}^{N_d} I(\mathbf{x})_m \omega_m$, within the berlingot-shaped medium of the tests 2A to 2E. Adhering to the physics we can clearly notice, in the provided cross-sections, pure transport, absorption dominance,



(a) Test 2A, transparent medium without reflection.



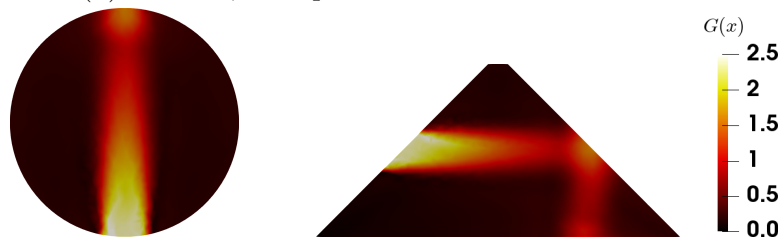
(b) Test 2B, highly absorbing medium without reflection.



(c) Test 2C, highly scattering medium without reflection.



(d) Test 2D, transparent medium with reflection.



(e) Test 2E, highly scattering medium with reflection.

Figure 5: Radiation density cross-sections for the berlingot-shaped medium tests.

Test	κ	σ_s	n	Comments
2A	ϵ	ϵ	1	Transparent medium without reflection
2B	5	ϵ	1	Highly absorbing medium without reflection
2C	ϵ	5	1	Highly scattering without reflection
2D	ϵ	ϵ	2.5	Transparent medium with reflection
2E	ϵ	5	2.5	Highly scattering with reflection

Table 2: Radiative properties for tests 2A to 2C used in section 4.2: the absorption coefficient κ (in cm^{-1}), the scattering coefficient σ_s (in cm^{-1}), and the index of refraction n of the medium. The small value ϵ is set to 10^{-6} .

scattering dominance, and reflection dominance, for the respective tests.

Figures 6 to 10 present the convergence history of the GMRES and the BiCGSTAB used for solving tests 2A to 2E. For each case we have used the Krylov subspace solvers with and without preconditioners. From all these figures one can clearly draw a conclusion that the BiCGSTAB outperforms the GMRES in all cases. However, the BiCGSTAB is observed to show erratic behaviors of convergence ($\|r_k\|_2$ grows several order in magnitude) which is classic to this method. Axelsson [33] claims that Lanczos-based methods, such as the BiCGSTAB, being not based on minimization principles, are susceptible to erratic convergence behaviors. Such erratic behaviors were also reported in [34, 35]. These convergence outbursts are in fact caused by the near failure of the mutual orthogonalization process of the BiCGSTAB. We further show that these outbursts have less impact (almost negligible) for absorbing medium problems due to their lower condition numbers, while these are frequently present in other problems that are not absorption dominant. The outbursts in problems involving reflections are highest in number due to their weak conditioning. As it may occur, the BiCGSTAB may fail once in a while due to its delicate orthogonalization, hence its chances of failure for problems involving reflections is higher than for other problems. On the contrary, the GMRES smoothly converges to the desired solutions, however with slower rates of convergence than the BiCGSTAB. Apart from the faster convergence rates of the BiCGSTAB, it should also be noted that, the BiCGSTAB uses less memory than the GMRES. This is because 30 additional auxiliary vectors (the maximum dimension of the Krylov subspace generated by the Arnoldi procedure before a restart occurs) need to be stored for the GMRES compared to the BiCGSTAB which uses a short recurrence

and only requires 8 auxiliary vectors.

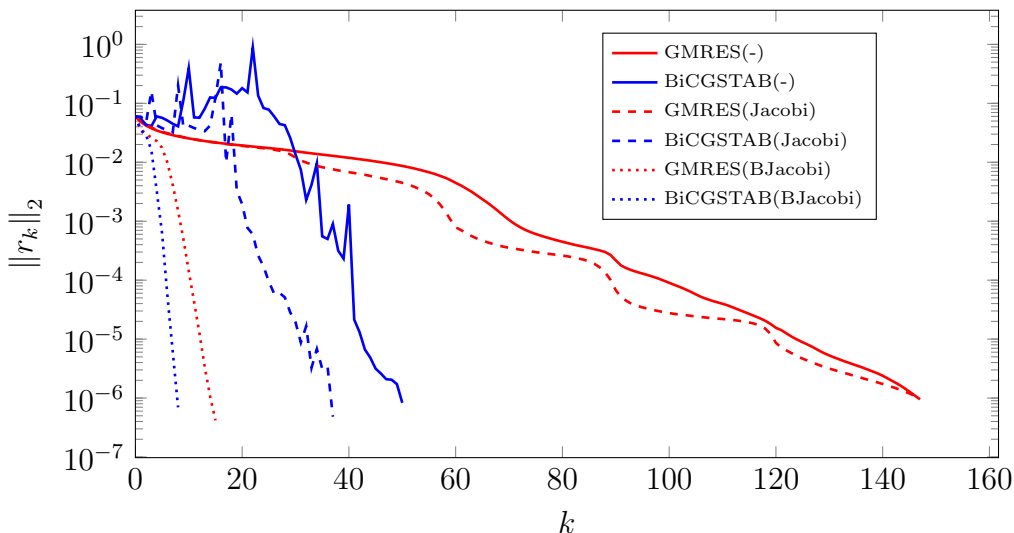


Figure 6: Logarithmic convergence history for the GMRES and the BiCGSTAB methods used for solving the transparent medium problem without reflection, test 2A. Block Jacobi is abbreviated as BJacobi.

In all convergence history plots, it is clear that both Jacobi and block Jacobi preconditioners reduce the total iteration counts for both Krylov subspace methods. It can also be observed that preconditioning in case of the BiCGSTAB not only leads to faster convergences but also stabilizes the method.

In table 3 we provide the total number of iterations to converge k_c and the respective times to solution t_s for tests 2A to 2E. The reported times t_s correspond to the time spent in setting up the preconditioner plus for reaching convergence. The table displays that much more work is required for solving the problems involving reflection. All expect one result are adhering to the eigenvalue analysis carried out in the previous section. The result that does not agree with the previous eigenvalue analysis is the transparent case with reflection, test 2D. The higher iteration count (compared to other tests in this subsection), may mean that this test has a worst eigenspectrum distribution than the others. While this was not the case for the cubic-shaped test case. We observed such a behavior because, unlike the cubic-shaped media that has six unique normals, the berlingot-shaped media has 455 unique normals at

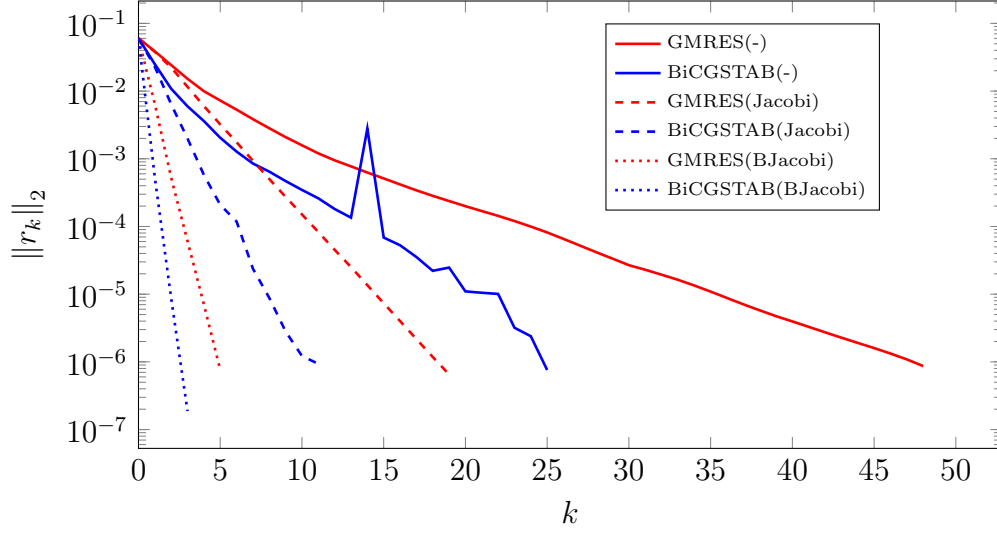


Figure 7: Logarithmic convergence history for the GMRES and the BiCGSTAB methods used for solving the absorbing medium problem without reflection, test 2B. Block Jacobi is abbreviated as BJacobi.

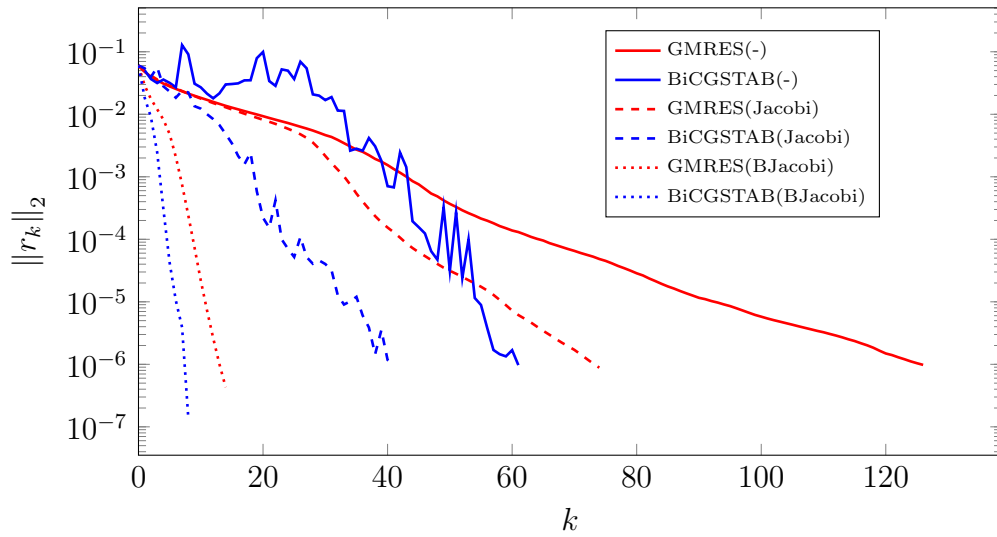


Figure 8: Logarithmic convergence history for the GMRES and the BiCGSTAB methods used for solving the scattering medium problem without reflection, test 2C. Block Jacobi is abbreviated as BJacobi.

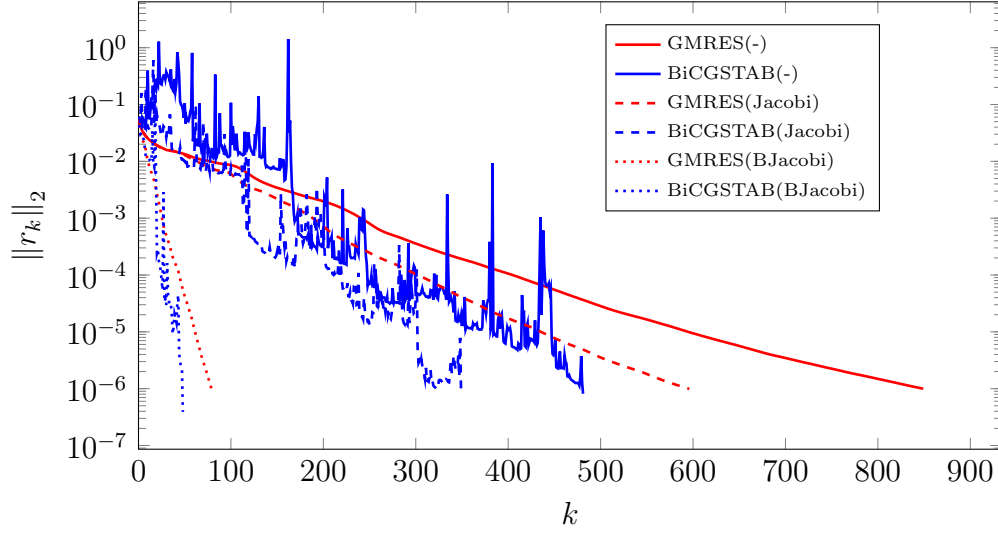


Figure 9: Logarithmic convergence history for the GMRES and the BiCGSTAB methods used for solving the Transport problem with reflection, test 2D. Block Jacobi is abbreviated as BJacobi.

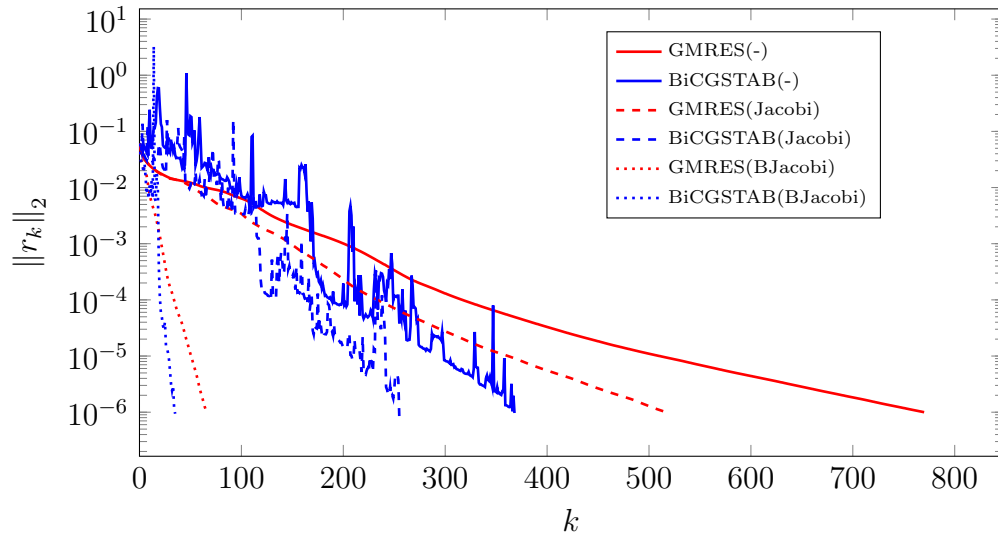


Figure 10: Logarithmic convergence history for the GMRES and the BiCGSTAB methods used for solving the scattering medium problem with reflection, test 2E. Block Jacobi is abbreviated as BJacobi.

the boundary (mesh dependent). Because of the transparency, no resistance is offered to the incoming radiation ($\kappa = \sigma_s \approx 0$), this radiation will remain trapped in the medium for a longer period and each time it hits any surface different angles get coupled with each other. Hence, the coupling is arbitrary and much more complex compared to the cubic-shaped reflection cases.

Test	GMRES						BiCGSTAB					
	None		Jacobi		BJacobi		None		Jacobi		BJacobi	
	k_c	t_s	k_c	t_s	k_c	t_s	k_c	t_s	k_c	t_s	k_c	t_s
2A	147	88.1	147	84.17	15	9.2	50	56.5	37	41.6	8	9.8
2B	48	34.5	19	10.9	5	4.0	25	27.3	11	6.0	3	2.0
2C	126	70.8	74	60.1	14	8.1	61	50.7	41	44.9	9	4.0
2D	849	496.10	596	366.47	79	45.1	481	369.7	349	260.4	48	41.01
2E	770	445.6	517	292.2	66	57.1	368	310.4	255	200.8	35	34.01

Table 3: Performance in terms of iterations to converge (k_c) and solving time (t_s , in seconds), for the GMRES and the BiCGSTAB with/without preconditioners.

Overall, in this subsection, the BiCGSTAB was seen to outrun the GMRES, for solving different problems of radiation, in terms of convergence rates, total solving times, and memory requirements.

5. Conclusion

This article was dedicated to the analysis of Krylov subspace methods for solving different multi-dimensional radiative transfer problems. The radiative transfer phenomena in these problems is modeled using the discrete ordinates radiative transfer equation. The linear systems for these different multi-dimensional radiative transfer problems were built following the angular decomposition (with mixed finite elements) discretization of the discrete ordinates radiative transfer equation.

Based on the physics, radiation in transparent, absorbing, scattering, and reflecting media were analyzed. An eigenspectrum analysis was set up on these different problems in order to study the effect of each physics on the condition number of the problem. It was concluded that: absorbing/transparent media problems are well conditioned, including scattering decreases the condition number of the discretized system, condition numbers for absorbing and reflecting media do not change, and conditioning deteriorates heavily when reflection is involved in transparent/scattering medium problems.

Two Krylov subspace solvers, the GMRES and the BiCGSTAB, with and without preconditioning, were investigated for solving the above mentioned radiative transfer problems. In conclusion, the BiCGSTAB outran the GMRES for all cases, with lower iteration count, solving times, and memory requirements. However, typical to the BiCGSTAB, erratic convergences were sometimes observed in comparison to the smooth convergence curves for the GMRES. These erratic behaviors were more prominent for the cases with reflecting media. Concerning preconditioners, as expected, it was established that preconditioning systems with the block Jacobi method (with incomplete LU factorizations with zero level of fill-in as block solvers) leads to faster convergence. Moreover, preconditioning also reduced drastically the outbursts of the BiCGSTAB.

Acknowledgements

M. A. Badri would like to thank IRT JV (French Institute in Research and Technology in Advance Manufacturing Technologies for Composite, Metallic and Hybrid Structures) for funding his research. The authors also thank the Institute of Intensive Computation (ICI, Centrale Nantes, France), for granting an access to their supercomputers.

References

- [1] M. F. Modest, Radiative heat transfer, Academic press, 2013.
- [2] G. Krishnamoorthy, R. Rawat, P. J. Smith, Parallelization of the p_1 radiation model, Numerical Heat Transfer, Part B: Fundamentals 49 (2006) 1–17.
- [3] L. Ruan, W. An, H. Tan, H. Qi, Least-squares finite-element method of multidimensional radiative heat transfer in absorbing and scattering media, Numerical Heat Transfer, Part A: Applications 51 (2007) 657–677.
- [4] Y. Lu, A. F. Chatziioannou, A parallel adaptive finite element method for the simulation of photon migration with the radiative-transfer-based model, Communications in numerical methods in engineering 25 (2009) 751–770.
- [5] D. Balsara, Fast and accurate discrete ordinates methods for multidimensional radiative transfer. Part I, basic methods, Journal of Quantitative Spectroscopy and Radiative Transfer 69 (2001) 671–707.
- [6] D. Le Hardy, Y. Favennec, B. Rousseau, Solution of the 2-D steady-state radiative transfer equation in participating media with specular reflections using SUPG and DG finite elements, Journal of Quantitative Spectroscopy and Radiative Transfer 179 (2016) 149–164.
- [7] W. Fiveland, Discrete-ordinates solutions of the radiative transport equation for rectangular enclosures, Journal of Heat Transfer 106 (1984) 699–706.
- [8] D. Boffi, F. Brezzi, M. Fortin, Mixed finite element methods and applications, volume 44 of springer series in computational mathematics, 2013.
- [9] D. Le Hardy, M. A. Badri, B. Rousseau, S. Chupin, D. Rochais, Y. Favennec, 3D numerical modelling of the propagation of radiative intensity through a X-ray tomographed ligament, Journal of Quantitative Spectroscopy and Radiative Transfer 194 (2017) 86–97.

- [10] O. Lehtikangas, T. Tarvainen, A. Kim, S. R. Arridge, Finite element approximation of the radiative transport equation in a medium with piecewise constant refractive index, *Journal of Computational Physics* 282 (2015) 345–359.
- [11] D. Le Hardy, Y. Favennec, B. Rousseau, F. Hecht, Specular reflection treatment for the 3D radiative transfer equation solved with the discrete ordinates method, *Journal of Computational Physics* 334 (2017) 541–572.
- [12] W. An, L. Ruan, H. Qi, L. Liu, Finite element method for radiative heat transfer in absorbing and anisotropic scattering media, *Journal of Quantitative Spectroscopy and Radiative Transfer* 96 (2005) 409–422.
- [13] M. Badri, P. Jolivet, B. Rousseau, S. Le Corre, H. Digonnet, Y. Favennec, Vectorial finite elements for solving the radiative transfer equation, *Journal of Quantitative Spectroscopy and Radiative Transfer* 212 (2018) 59–74.
- [14] M. A. Badri, P. Jolivet, B. Rousseau, Y. Favennec, High performance computation of radiative transfer equation using the finite element method, *Journal of Computational Physics* (2018).
- [15] D. Mihalas, *Stellar atmospheres*, San Francisco, WH Freeman and Co., 1978. 650 p. (1978).
- [16] M. L. Adams, E. W. Larsen, Fast iterative methods for discrete-ordinates particle transport calculations, *Progress in nuclear energy* 40 (2002) 3–159.
- [17] E. W. Larsen, Transport acceleration methods as two-level multigrid algorithms, *Operator Theory: Advances and Applications* 51 (1991) p34–47.
- [18] I. C. Ipsen, C. D. Meyer, The idea behind Krylov methods, *American Mathematical Monthly* (1998) 889–899.
- [19] S. Turek, A generalized mean intensity approach for the numerical solution of the radiative transfer equation, *Computing* 54 (1995) 27–38.

- [20] M. Seaid, M. Frank, A. Klar, R. Pinnau, G. Thömmes, Efficient numerical methods for radiation in gas turbines, *Journal of Computational and Applied Mathematics* 170 (2004) 217–239.
- [21] B. W. Patton, J. P. Holloway, Application of preconditioned GMRES to the numerical solution of the neutron transport equation, *Annals of Nuclear Energy* 29 (2002) 109–136.
- [22] W. F. Godoy, P. E. DesJardin, On the use of flux limiters in the discrete ordinates method for 3D radiation calculations in absorbing and scattering media, *Journal of Computational Physics* 229 (2010) 3189–3213.
- [23] S. Balay, S. Abhyankar, M. F. Adams, J. Brown, P. Brune, K. Buschelman, L. Dalcin, V. Eijkhout, W. D. Gropp, D. Kaushik, M. G. Knepley, L. C. McInnes, K. Rupp, B. F. Smith, S. Zampini, H. Zhang, H. Zhang, PETSc web page, 2017.
- [24] M. A. Heroux, R. A. Bartlett, V. E. Howle, R. J. Hoekstra, J. J. Hu, T. G. Kolda, R. B. Lehoucq, K. R. Long, R. P. Pawlowski, E. T. Phipps, et al., An overview of the Trilinos project, *ACM Transactions on Mathematical Software (TOMS)* 31 (2005) 397–423.
- [25] H. A. Van der Vorst, Bi-CGSTAB: A fast and smoothly converging variant of Bi-CG for the solution of nonsymmetric linear systems, *SIAM Journal on scientific and Statistical Computing* 13 (1992) 631–644.
- [26] Y. Saad, M. H. Schultz, GMRES: A generalized minimal residual algorithm for solving nonsymmetric linear systems, *SIAM Journal on scientific and Statistical Computing* 7 (1986) 856–869.
- [27] W. E. Arnoldi, The principle of minimized iterations in the solution of the matrix eigenvalue problem, *Quarterly of applied mathematics* 9 (1951) 17–29.
- [28] M. Avila, R. Codina, J. Principe, Spatial approximation of the radiation transport equation using a subgrid-scale finite element method, *Computer Methods in Applied Mechanics and Engineering* 200 (2011) 425–438.
- [29] W. H. Reed, New difference schemes for the neutron transport equation, *Nuclear Science and Engineering* 46 (1971) 309–314.

- [30] Y. Saad, Iterative methods for sparse linear systems, SIAM, 2003.
- [31] L. G. Henyey, J. L. Greenstein, Diffuse radiation in the galaxy, The Astrophysical Journal 93 (1941) 70–83.
- [32] F. Robert, E. Alain, Berlingot, <http://www.mathcurve.com/surfaces/berlingot/berlingot.shtml>, 2017.
- [33] O. Axelsson, Iterative solution methods, Cambridge university press, 1996.
- [34] G. Kanschat, Solution of radiative transfer problems with finite elements, in: Numerical methods in multidimensional radiative transfer, Springer, 2009, pp. 49–98.
- [35] S. Turek, An efficient solution technique for the radiative transfer equation, Impact of computing in science and engineering 5 (1993) 201–214.